EXPERIMENTAL AND NUMERICAL STUDY OF CAVITATION IN HEADFORM CONFIGURATIONS

Aviad Gofer[1], Shlomy Shitrit[2]
RAFAEL, Advanced Defense Systems, Ltd., Haifa 31021, Israel
RAFAEL, Advanced Defense Systems, Ltd., Haifa 31021, Israel

Nomenclature

ρ	=	density, kg/m^3
D	=	head form diameter, m
L	=	headform length, m
μ_v, μ_l	=	vapor and liquid molecular viscosity, kg/ms
u, v, w	=	velocity components, m/s
p	=	static pressure, Pa ; order of convergence
R	=	residual
Rey	=	Reynolds number
σ	=	Cavitation number
$y+$	=	yplus
Cd	=	Drag coefficient
α_v	=	vapor volume fraction
α_l	=	liquid volume fraction
ρ_v	=	vapor density
ρ_l	=	liquid density
p_{sat}	=	water saturation pressure
R_e, R_c	=	mass exchange rate
C_{dest}, C_{prod}	=	Kunz's cavitation model empirical constants

GCI	=	grid convergence index
N	=	mesh size
L	=	grid level

Subscripts

baseline	=	initial configuration
ref	=	reference value

Abstract

[1] Research Engineer, Hydro group, Aeronautical Systems, P.O. Box 2250; aviad.gofer@gmail.com
[2] Research Engineer, CFD group, Aeronautical Systems, P.O. Box 2250; shlomy.shitrit@gmail.com

A novel facility was constructed for investigating the motion of high-speed underwater bodies. The testing facility consists of a pneumatic piston capable of accelerating a specially designed underwater body to speeds as high as 30 m/s, hence achieving the cavitation range. The body maintains an approximately constant velocity for a few tens of milliseconds. Preliminary experimental work was performed to evaluate the performance of the novel testing equipment, using a high-speed camera to analyze different geometries at different velocities. Results showed good agreement in terms of cavitation bubble size when compared with numerical calculations using CFD.

I. Introduction

High-speed underwater bodies deal with cavitation and super-cavitation phenomena.

Cavitation phenomenon is associated with vapors appearing within a liquid due to a local decrease in pressure to a level equal or below the equilibrium vapor pressure. Typically, it relates to propellers or pumps, where this phenomenon is undesirable due to erosion and damage caused by the collapse of the bubbles. In high speed underwater vehicles a cavitation bubble originating at the nose may elongate and envelope the entire body. Such situation is termed “super cavitation” and may be used purposefully to substantially reduce hydrodynamic drag, enabling noticeably higher motion velocity. The Russians were the first to take advantage of the super cavitation phenomena, constructing and deploying a super cavitation torpedo (Shkval) that can move underwater at speeds as high as 400 km/h, an order of magnitude faster than common marine vehicles.

Until recently only little knowledge and practically no development in this area have been acquired in Israel. The objective of this research is to investigate the dynamic and hydrodynamic behavior of a high-speed underwater vehicle in the presence of a cavitation bubble. This goal requires the characterization of a cavitation/super cavitation bubble formed over a moving body and investigation of the stability of both the body and bubble as a function of speed, angle of attack, shape of body and nose, and scale, as well as other parameters such as gas injection to enhance stabilization and shaping the bubble artificially.

Rafael has developed a unique high motion speed pneumatic piston driven facility, capable of similar features for short times and having in addition force and moment measuring capability in all directions, which is very significant for characterizing the loads that can lead to instability.

Successfully predicting cavitation and its negative effects (e.g. thrust breakdown in propellers) or positive effects, (e.g. when drag reduction is involved) is increasingly important at the development process. It is crucial to predict and model cavitation, and this is where computational fluid dynamics (CFD) becomes a powerful tool. Compared to the cost of running large water tunnel, the preparation time and constructing complex scale models, the computational solution provides a cheap, valuable and efficient solution. However, the drawback to computational solutions is that they are only approximations of the real flow. While CFD provides fairly accurate solutions to real life problems, it still must be validated by experimental results, and this type of validation is crucial for development in both fields.

II. Scientific background

The stability of a super cavitation bubble relates directly to the bubble shape and dimensions, which are further dependent on the vessel shape and the flow and pressure fields. The length of the super cavitation bubble is one of the most important parameters of the bubble shape. It is measured from the separation point to the closure point (the rearmost point of the bubble). Experiments have shown that it is associated by many uncertainties due to the instability of the

bubble boundaries. The bubble length grows with the decrease of the relative sub pressure σ_c. For small values of the relative sub pressure σ_c, there is an empirical correlation between the length of the bubble and the relative sub pressure [1]:

$$\frac{l}{c} \cong A\sigma_c^{-n} \qquad \textbf{(1)}$$

Where c - the characteristic size of the body, l - length of the bubble. It is found that for a body located in an infinite medium the value of the exponent n is 2. The value of the coefficient A is dependent on the location and form of the body. It is possible to see that for values of $\sigma_c \to 0$, the bubble is infinite.

The most basic relations are derived from Garbedian (1956) [2] asymptotic model for continuous super cavitation, for cases in which the gravity force is negligible and for small enough values of the relative pressure of the bubble σ_c (where characteristic values are $\sigma_c < 0.1$). The bubble takes the form of an ellipsoid whose length l and maximum diameter d_c as a function of σ_c:

$$\begin{cases} \dfrac{d_c}{d} = \sqrt{\dfrac{C_D}{\sigma_c}} \\ \dfrac{l_c}{d} = \dfrac{1}{\sigma_c}\sqrt{C_D \ln\left(\dfrac{1}{\sigma_c}\right)} \end{cases}, \qquad \textbf{(2)}$$

where d is the diameter of the cavity, C_D is the drag coefficient.

The super cavitation flow problems are governed by several dimensionless coefficients that affect the scaling in the super cavitation research and application design. The main coefficients commonly used are the cavitation number σ and the pressure coefficient $C_{p,\min}$. The cavitation number depends on the flow conditions, and the pressure coefficient depends on the body shape. They both satisfy the relation:

$$\frac{l}{d} \propto \left(-\sigma - C_{p,\min}\right) \qquad \textbf{(3)}$$

Most researchers usually use the under pressure coefficient which depends on the actual cavity pressure instead of the vapor pressure, as the cavitation number does [1].

Reynolds number is also an important dimensionless coefficient which can affect the boundary layer and thus the entire flow. Its effect appears in a viscous flow, and thus in the scaling examination [3].

III. Experiment System

The unique test facility has a new concept, which was designed and constructed in-house. The system consists of a submerged body mounted on a pneumatic piston. During a 1-m movement of the piston it can reach a velocity of 30 m/s, maintaining constant speed for a 70-cm displacement (about 20-30 ms duration). The body can be of different shape and size with different cavitator (nose) geometries. It can also provide different angles of attack as well as air injection at any location on the examined body. Transparent wall allows excellent visual access for high speed photography of the moving body and the development of a cavitation bubble. The basic system already exists, and preliminary experiments have been conducted,

revealing the formation of a cavitation bubble around the body when reaching a speed of 30 m/s. Schematic of the system is presented in Fig. 2. And Fig. 3.

The unique of the facility is the ability to reach high velocities in a large test cross-section area. It is achieved by moving the body in a constant velocity instead of creating a uniform free stream facing a stationary body. High velocities free stream in water flow involves very high mass flow rate (30 ton/s for velocity of 30m/s in a 1[m^2] cross-section area). As can be seen in Fig. 1, high-speed cavitation test facilities in the world are characterized with small cross-section area.

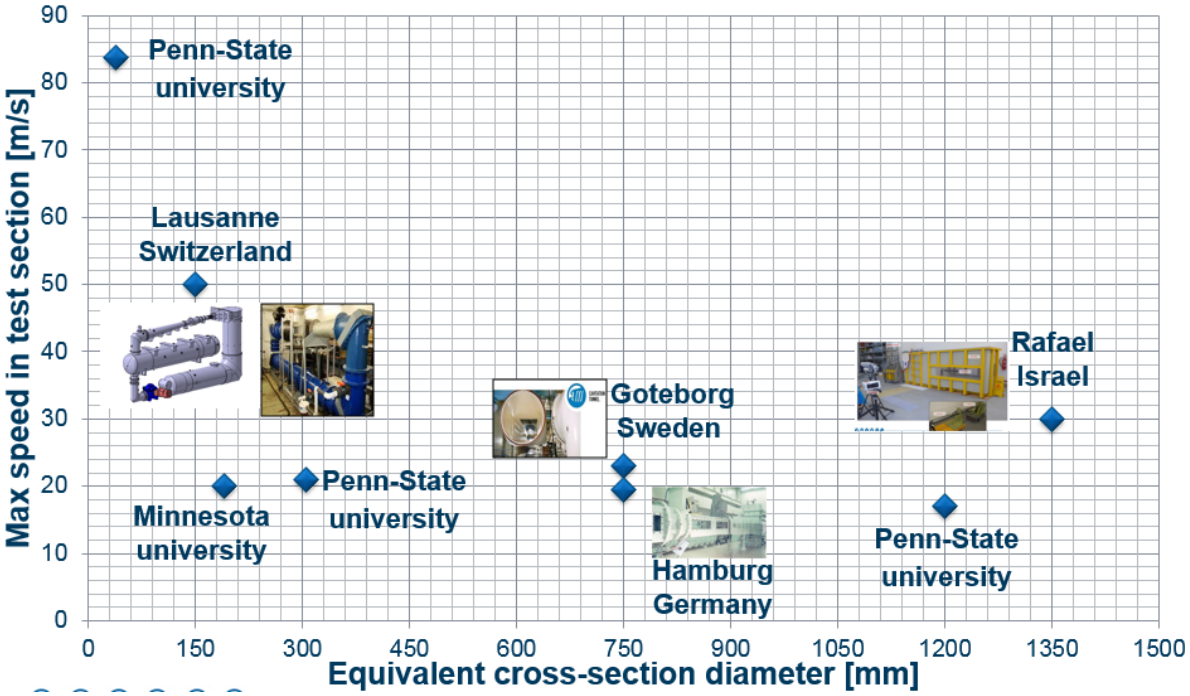

Fig. 1. Characteristics of cavitation tunnels in the world

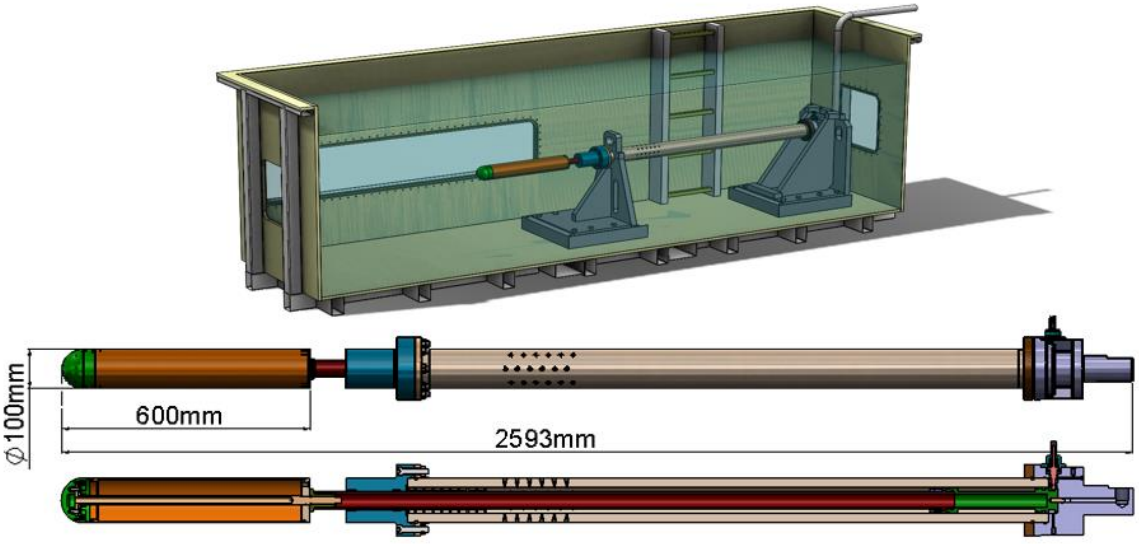

Fig. 2. Schematic of Rafael's pneumatic piston test system

Fig. 3. Rafael's pneumatic piston test system

IV. Experiment Results

Experiments were done with different nose configurations and in different velocities. Results were examined with high-speed phantom camera taking 10,000 frames per second. High-speed photography analysis showed constant velocity during majority part of the piston movement. The velocity analysis can be seen in Fig.4.

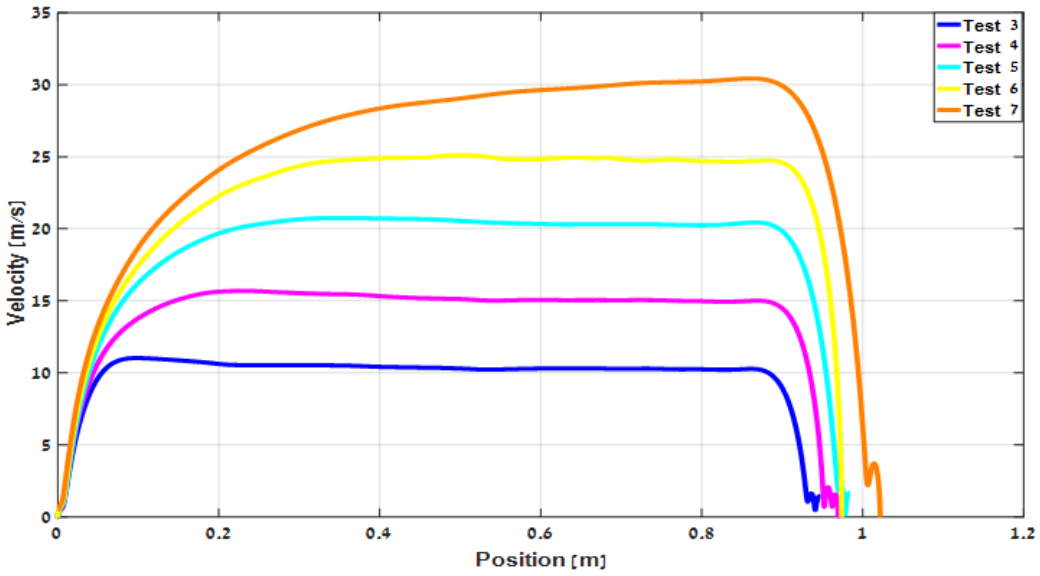

Fig. 4. High-speed photography piston velocity analysis

The results shown in Fig.5 were found for body velocity of 30m/s and different noses. It can be seen that the longest bubble is created for hemisphere nose (nose 1) and becomes smaller when the nose become more elliptic (as expected) due to smaller accelerations along the body. The big difference in bubble size at a given body velocity can be seen in Fig.6.

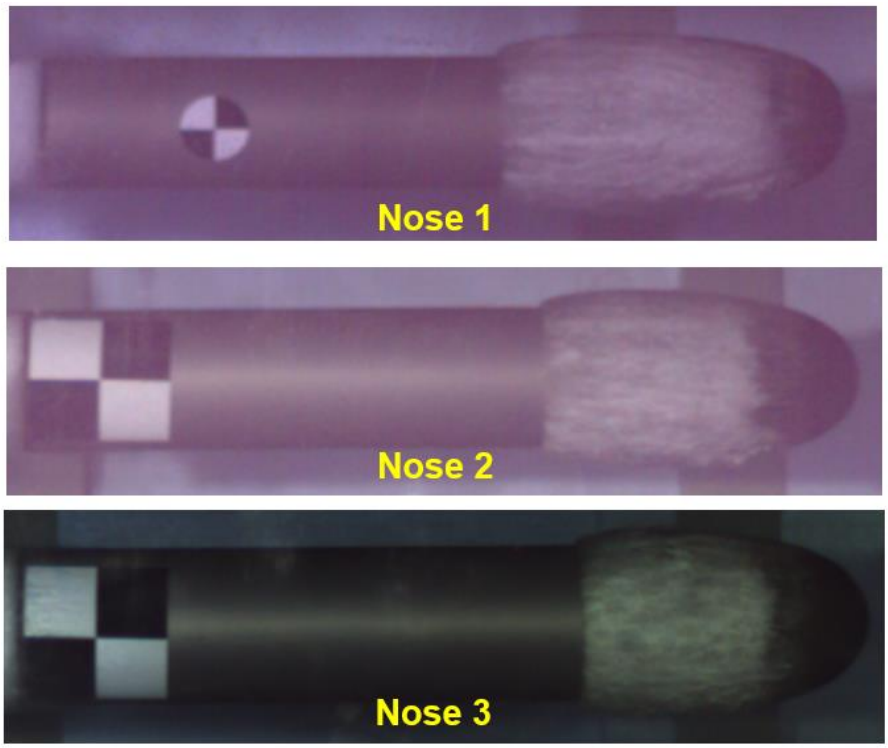

Fig. 5. Test results for Cavitation bubble length for different noses

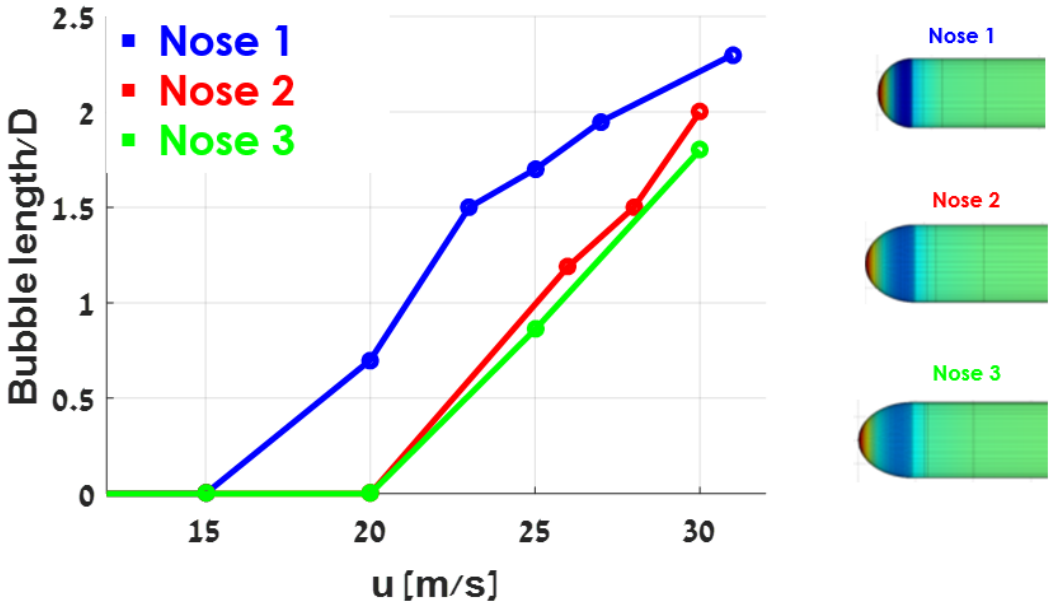

Fig. 6. Normalized cavitation bubble length as a function of body velocity, for different noses

V. Numerical modeling

The equations solved are the Reynolds Averaged Navier-Stokes (RANS) equations. An incompressible segregated flow model is selected solving the integral conservation equations of mass and momentum is sequential manner. An Eulerian multiphase model is used, treating the fluid as a single continuum (Volume of Fluid (VOF) method), assuming a no-slip condition between liquid and vapor phase, with varying properties in space according to its composition. The volume fraction of the components is determined from the condition, $\alpha_v + \alpha_l = 1$, where α_v and α_l are the vapor and liquid volume fraction respectively. The mixture density and viscosity are defined as $\rho = \alpha_v \rho_v + \alpha_l \rho_l$ and $\mu = \alpha_v \mu_v + \alpha_l \mu_l$ respectively.
The k-epsilon turbulence model is used to describe the turbulent viscosity [4]. The cavitation number is defined as $\sigma = (p_\infty - p_{sat})/(0.5\rho_l {v_\infty}^2)$ where p_∞ is the farfield pressure, p_{sat} is the liquid saturation pressure, and v_∞ is the velocity of the free stream.

A. CFD solver-interPhaseChangeFoam

The interPhaseChangeFoam is a solver for two incompressible, isothermal immiscible fluids with phase change that incorporates Volume-of-fluid (VOF) phase-fraction based interface capturing approach. The fluid properties of the mixture is solved by one momentum equation. Three phase change models are included (Kunz, Merkle and Schnerr-Sauer). The volume fraction equation that includes source terms to account for mass transfer, is solved by multidimensional-universal-limiter-with-explicit-solution (MULES) method. The homogenous equilibrium model states that the velocity, temperature and pressure between the phases are equal. With this state we assume that momentum, energy and mass transfer are fast enough to reach equilibrium.

B. Cavitation model –Kunz model

The model by Kunz [5], [6] was developed for sheet and super cavitating flows. Sheet cavitation is known to have a gas-liquid interface which is nearly in dynamic equilibrium and pressure and velocity over the interface do not vary heavily. Kunz et al. [7] solved separate continuity equations for the liquid and vapor phases with the objective of modeling of submerged bodies subjected to natural cavitation. The conservative form of the liquid-volume fraction equation is:

$$\frac{\partial \rho_i \alpha_i}{\partial t} + div(\rho_i \bar{u} \alpha_i) = div\left(\gamma \nabla \frac{\rho_i}{\bar{\rho}} \alpha_i\right) + R_e - R_c \tag{4}$$

Where R_e and R_v are the mass exchange rates, and gama is known as the effective exchange rate coefficient. In Kunz cavitation model, the transition from vapor to liquid R_e is modeled linearly with pressure and liquid fraction. Liquid to vapor change R_c a simplified Ginzburg-Landau relationship is used.

$$R_e = \frac{C_{dest} \rho_v \alpha_l \min[0, p - p_{sat}]}{\rho_l \frac{{u_\infty}^2}{2} t_\infty} \tag{5}$$

$$R_c = \frac{C_{prod} \rho_v {\alpha_l}^2 (1 - \alpha_l)}{t_\infty} \tag{6}$$

The free stream velocity is U_∞ and t_∞ is the free stream time scale (D/U_∞). The coefficients used in the following study are: $Cdest = 1000$, $Cprod = 1000$.

Hemispherical headform model for validation

In order to increase the confidence in the numerical experiments, and in order to quantify the cavitation model parameters, we decided to first validate the simulation system with the work performed by Rouse and McNown at the University of Iowa in the late 1940's [8]. This hemispherical headform model has been studied in depth over the years, and has excellent experimental data with which to compare. The hemispherical headform is studied in two cases, single phase and multiphase including the phase change process by using the Kunz cavitation model. This validation case is twofold: First, to assess the accuracy of the solver to match experimental quantity values such as coefficient pressure distribution. Second, to study the effectiveness of the mesh resolution and also calibrate the cavitation model parameters. The computational domain, which illustrate the boundary conditions, and mesh used are shown in Figure 7.

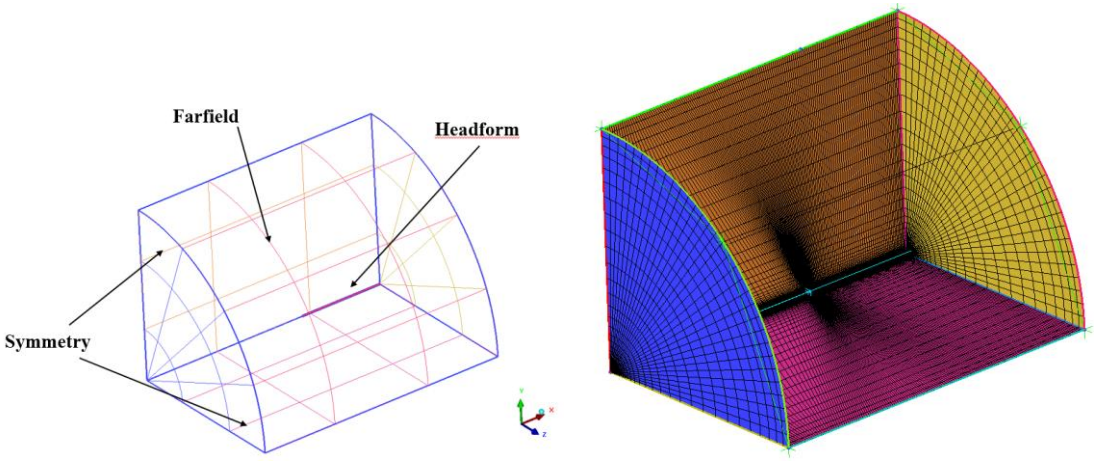

Fig. 7. Left: Computational domain. Right: Structured mesh.

C. Flow parameters and numerical setup

The headform model has a ball shaped nose with a diameter $D = 25.4$ mm and total length of $L = 50$. The computation domain is presented in Fig. . The inlet velocity was set to 8.27 m/s to yield a Reynolds number of $Rey = 2.1 * 10^5$. This study was solved with k-epsilon turbulence model and were designed with a $y^+ \approx 10$. The turbulence variables k and epsilon set to 0.01025 m^2/s^2 and 0.0672 m^2/s^3 respectively. At the exit plane, the pressure field was set to a fixed value of zero and zero gradient on the inlet and walls.

A structured grid is built using ICEMCFD commercial software, while the farfield is located $100D$ (see Fig.). The mesh topology includes 350,000 cells. The minimum cell size close to the boundary is $3 * 10^{-6}\ m$, reaching $y^+ \approx 1$. Grid convergence study was conducted while refining the grid in x, y and z directions. The experimental pressure coefficient distribution results along the headform is used as a measure for grid convergence. For the single phase configuration the steady state incompressible simpleFoam solver is used, and in order to ensure convergence the solution variables were set to tolerance of 10^{-6}.

D. Simulation results – cavitating and non-cavitating flow

The single phase (Fig.) and the multiphase (Fig.) simulation results are compared to experimental data published by Rouse and McNown in 1945. Fig. shows the pressure coefficient distribution along the headform with respect to the distance along the surface of the headform ('s'), normalized by the headform diameter D. It clearly seen that the head form single phase case performs closer to the experimental results compared to the multiphase case.

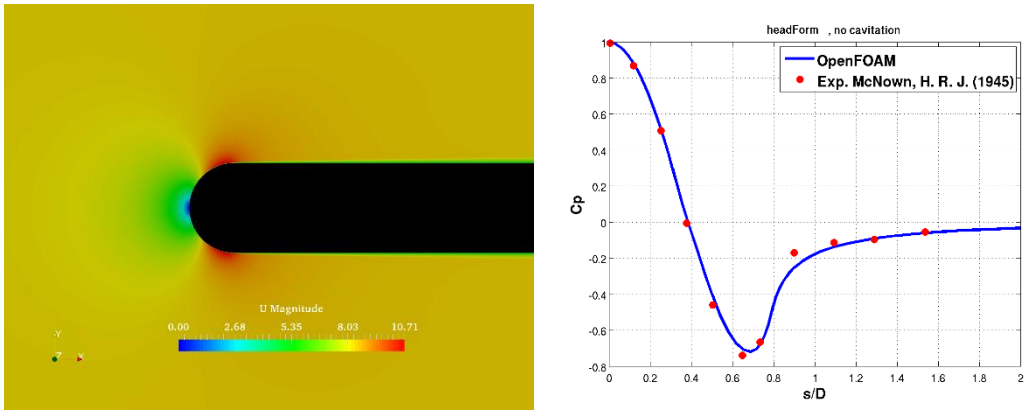

Fig. 8. Steady state simulation results of the single phase case. Left, velocity distribution on the symmetry plane. Right, Cp values with respect to the distance ('s') along the head form's surface, normalized by the diameter D

The multiphase case was tested using cavitation number of 0.4, and Kunz as the cavitation model. Based upon the single phase flow solution, the cavitation case used the converged single phase results to start the simulation in order to aid in convergence of the two phase solution. The incompressible solver (interPhaseChangeFoam) does not account for thermodynamic effects and therefore does not require a specified initial condition for the temperature. The density values supplied are 1000 Kg/m^3 for the water and 1.2 kg/m3 for air. The volume fraction was programmed as liquid, water having a value of 1 and vapor a value of 0. In terms of boundary conditions, the same parameters were used for the cavitation case as the single phase case. The only exception is that the Reynolds number has been set to 1.36*10^5 in order to match the flow field data from Rouse and McNown's cavitation case. The cavitation number is controlled by setting the farfield static pressure value as 15978 Pa.

The results of the liquid volume fraction distribution is presented in Fig. . Also a comparison of the Cp distribution along the surface, between the simulated and the experimental results. The OpenFOAM simulated results compares well with the experimental results, with slightly lower cavitation bubble length and lower peak in Cp. This peak in pressure is a result of flow towards the boundary in the vapor region. Further downstream, the pressure returns to the undisturbed free stream value. Almost an unsteady solver is involved, the pressure field has not been averaged over the time after reaching convergence.

As expected the cavity grows in length down the headform.

It is important to mention here that the interPhaseFoamSolver accounts for an acoustic Courant number as well as regular Courant number, both need to be limited to 1 in order to ensure convergence. The main effect of this issue is the small time step values needed to reach converged solution.

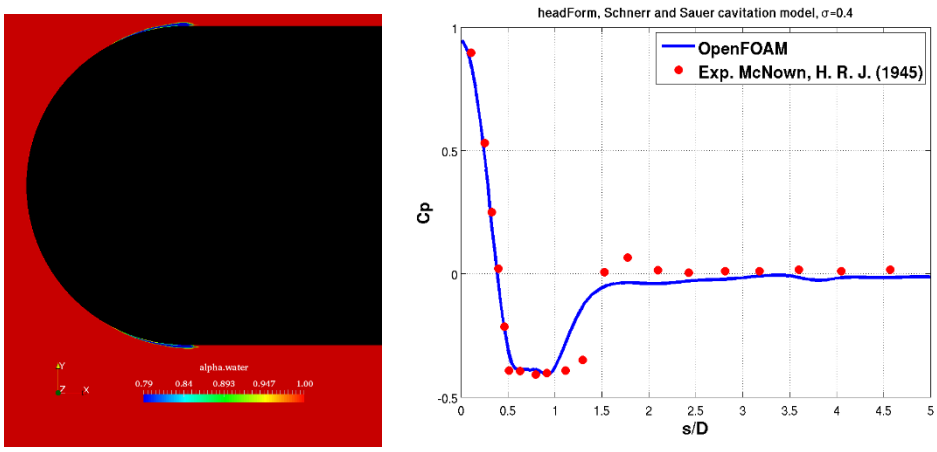

Fig. 9. Distribution of liquid volume fraction in the symmetry plane. The right figure is a comparison of the Cp values between simulation and experiments results. The distance along the head form's surface is represented by s, normalized by the diameter D

Validation of the experimental headform

E. Problem formulation

This study analyses the cavitation in three models characterized by three different nose part: Spherical, and two ogive types. The three models are characterized by the same 100 mm diameter and 600 mm cylinder's body length. The nose's geometry is given in Fig. , and we distinguish between the models as follows:

- Model 1: Spherical nose with origin located at the nose's tip.
- Model 2: Ogive type, while the tip of model 1 translated in 3 mm along the positive x direction.
- Model 3: Ogive type, while the tip of model 1 translated in 5 mm along the positive x direction.

The purpose of this study is to investigate the effect of the nose shape on the cavitation process and validate the solver by comparing to the experimental results.

In this case a full configuration is used and the computational domain, which is shown in Fig. , is large enough to minimize flow effects between model and boundaries. The farfield is located 30D in x, y and z directions. The left side of the grid is considered as a wall, the right side is outlet with fixed pressure value of 101325 Pa, and the top, bottom, front and back faces are considered as symmetry planes. No slip boundary condition was applied on the walls. In this case an unstructured hexahedral mesh cells were constructed by using the openFOAM built-in blockMesh and snappyHexMesh algorithm. The mesh consists of 745,000 cells with y+~10.

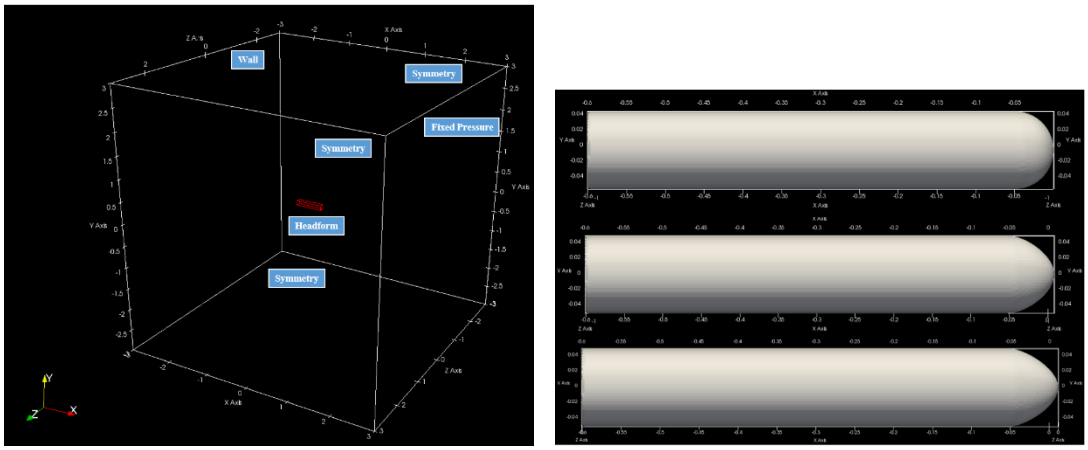

Fig. 10. Left: computational domain. Right: Comparison of the three computational models. From top to bottom: model 1, 2 and 3

F. Grid convergence study

The grid topology includes 763580 (level L0) cells. The minimum cell size close to the boundary is $3 * 10^{-6}\, m$, reaching $y^+ \approx 1$. Grid convergence study was conducted while refining the grid in x, y directions. The aerodynamic coefficients results of three different grid refinement levels are collected in

Table 1.

Grid convergence study has been made based on the Grid Convergence Index (GCI) method, for examining the spatial convergence of CFD simulations presented in the book by Roache. Roache suggests a GCI to provide a consistent manner in reporting the results of grid convergence studies and also an error band on the grid convergence of the solution. This approach is also based upon a grid refinement estimator derived from the theory of Richardson Extrapolation.

For the grid convergence study the problem solved is a static headform with water flow from right to left (in negative x direction) in a constant velocity of 20 m/s. The unsteady interFoam solver was used as the baseline with no phase change. InterFoam is a transient interface-capturing Navier-Stokes solver which is based upon the VOF and PISO methods. To ensure a converged solution, the variables in each case were set to a solution tolerance of $1 * 10^{-6}$.

The GCI values including the asymptotic range of convergence and an estimation of the drag coefficient values at zero grid spacing are detailed in Table 1. Based on this study we can say, for example, that Cd is estimated to be $Cd = 0.03210$ with an error band of 5.29%. The grid resolution studies confirmed that the computed pressure recovery coefficient is grid converged.

Table 1: Grid convergence study

Grid level (cells number)	Cd	Y+
L0-763580	0.0307974	1
L1-303676	0.0298764	6
L2-37564	0.0283052	10

Table 2: Pressure recovery coefficient in the grid convergence study

Grid level	Grid ratio, r	GCI [%]	Richardson extrapolation
L0	1	-	0.03210

C_d	L1	1.35	5.295	-
	L2	2.02	2.627	-

G. Head form's velocity profile

The motion of the simulated headform is designed to be accelerated axially (in x direction) from static state to 20 m/s constant velocity in 0.03 sec, approximately. The experimental velocity profile is presented in Fig. A summary of the incompressible cavitation solver constants used for the computational hemispherical headform cases can be seen in Table 3. The variables are the condensation empirical constant (Cc), the vaporization empirical constant (Cv), the mean flow time scale (t_∞), the velocity scale U_∞.

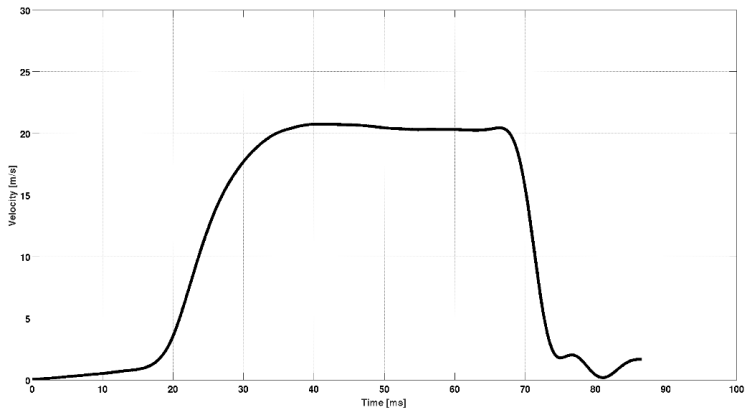

Fig.11. Designed axial motion of the headform

Table 3: Incompressible phase change model constants

Cavitation model	Cc	Cv	$U_\infty\ (\frac{m}{s})$	$t_\infty\ (sec)$
Kunz	1	1	20	0.005

Results and discussion

In Fig-14 the comparison between experimental (top images) and numerical (bottom images) results is presented, by a series of images, in four different times during the headform movement path. The final time is t=0.08 sec. In the bottom images the liquid volume fraction is presented, with values of 1 indicating water and 0 as vapor. The experimental results are presented in the top images, while the pocket cavitation process is clearly seen attached to the model's base and close to the nose. The volume fraction distribution is extracted in four time steps during the headform trajectory, from left to right and top to bottom: t=0.024 s, 0.04 s, 0.056 s, 0.072 s. The first series (Fig) represents model 1 (spherical nose), the second series (Fig.) of images compares the numerical and experimental results of model 2, and Fig. refers to model 3. As shown, in model 1, all three cases produce similar results in terms of volume fraction distribution.

In model 1, at t=0.024 s during the acceleration process, the simulated trailing cavity at the body's tail is bigger than that is shown in the experimental image. This may be caused by the fact that the experimental model is driven by a piston attached to the model's base and actually reduce the space where the cavitation occurs, and influence the dynamic cavitation at the rear

part of the model. This diagnostic repeated in the other ogive type models. At time t=0.04 s, at the end of the acceleration stage, where the headform moves in a constant velocity of approximately 20 m/s, the reduced pressure values along the nose causes form of trailing cavitation close to the front. As expected the cavities grow in length down the headform as time evolves, the cavity (at the front) fluctuates and eventually becomes disconnected. Another issue that can be clearly seen is that as the vapor cavities had reached full development, there were pressure fluctuations that skewed the liquid volume fraction field. This phenomena is clearly seen at time t=0.056 s, repeated in the three models. The pulsations cause the cavity to become broken and discontinuous, both at the front body and in the wake region. The last images of the first model, at time t=0.072 s, taken during the deceleration process, where the vapor pocket cavities keep moving in the center of mass velocity, and then the bubbles pocket collapse.

Since model 2 and 3 includes an ogive type nose, the flow along the nose accelerates to lower velocity values compared to the spherical nose, which results in moderate and much less intense cavities pockets. This sensitivity is clearly seen by the reduced sized pockets in the experimental model, and the smaller simulated trailing cavities. What is first evident is that the cavity length is fairly accurate in all cases and the Kunz model does a good job in predicting the size of the cavity pockets.

However, the main downfall, which is clearly visible in model 3, is that in the experimental model, no cavities where observed at the front body during the trajectory, whereas in the simulated model (3), cavities formation are clearly visible. Since the experimental process does not include any valuable data to compare (such as pressure values along the headform), the liquid volume fraction values are not known actually. Namely, by close looking at the bubbles pockets formation in the experimental images we cannot decide whether the pressure reduction region is over or under predicted. How close two objects (bubbles) can become before they blur into one? At absolute best humans eyes can resolve two lines 0.03 mm gap. In practice, objects 0.04 mm wide (the width of a human hair) are just distinguishable by good eyes, while objects below 0.02 mm wide are not. The cavitation bubbles size starts from around 0.001 mm, so there is a possibility that the cavities at the experimental front model really takes place, but is not visible by a standard image processing.

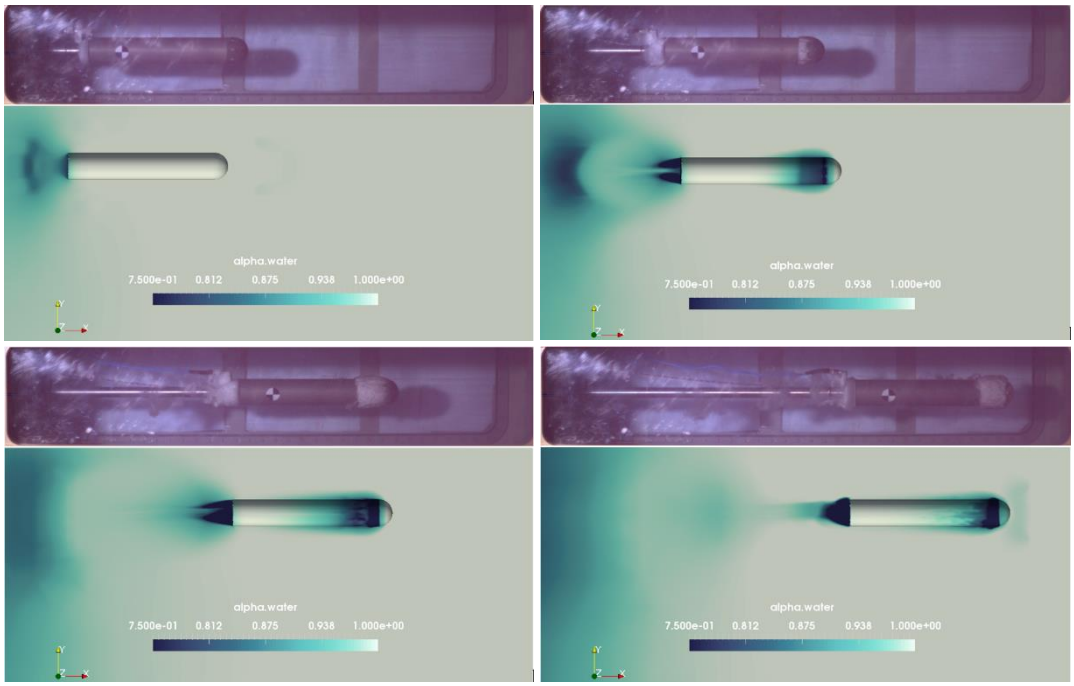

Fig. 12. Experimental images (at the top) and computational results (at the bottom) at four time values along the headform (model 1) motion. From left to right and top to bottom: t=0.024 s, 0.04s, 0.056s, 0.072s

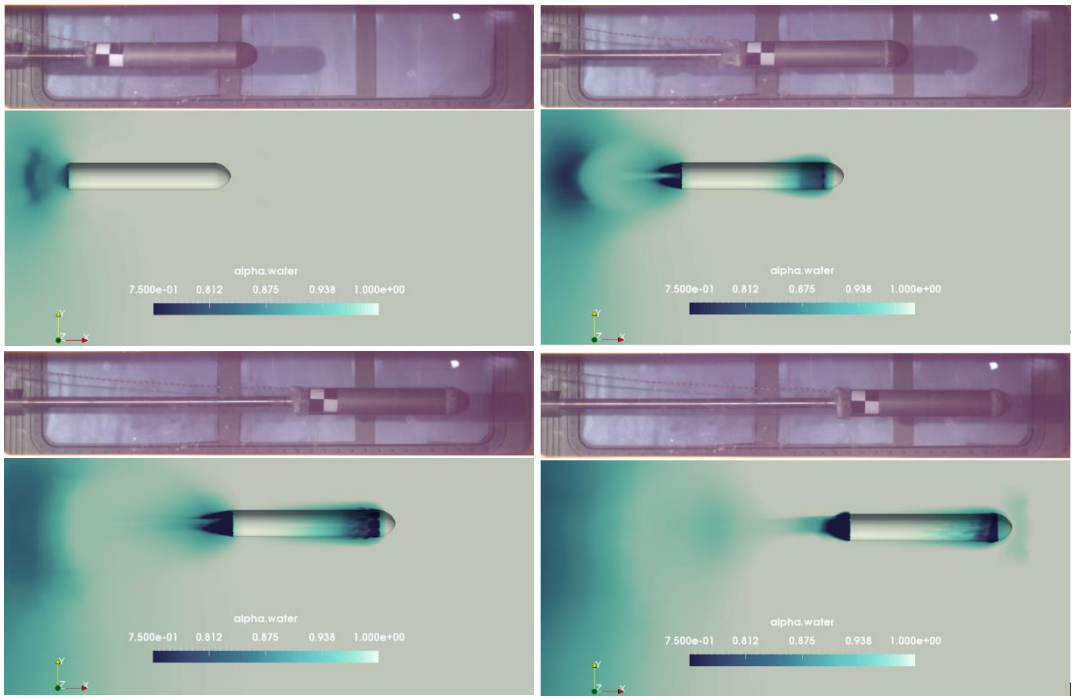

Fig. 13. Experimental images (at the top) and computational results (at the bottom) at four time values along the headform (model 2) motion. From left to right and top to bottom: t=0.024 s, 0.04s, 0.056s, 0.072s

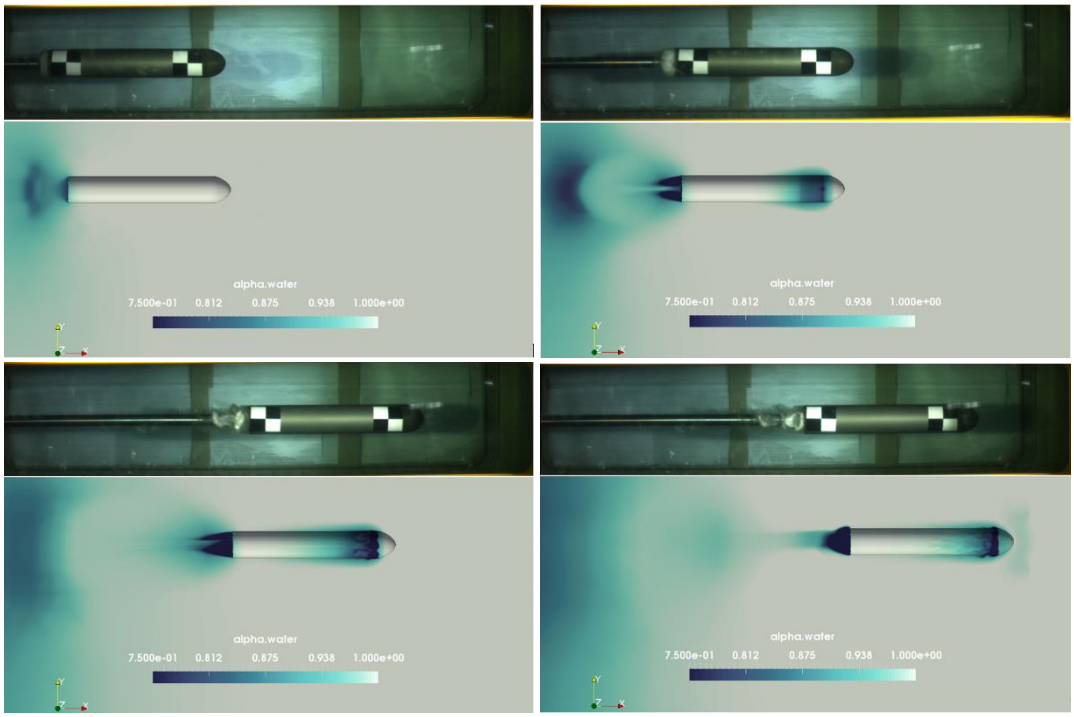

Fig. 14. Experimental images (at the top) and computational results (at the bottom) at four time values along the headform (model 3) motion. From left to right and top to bottom: t=0.024 s, 0.04s, 0.056s, 0.072s

In addition to the volume fraction distribution, an integral coefficient (such as drag, normal force or pitch moment) might be a useful tool to quantify the effect of the cavities, generated by the different nose geometries, on the overall drag generated by the model. For this purpose the integral drag coefficient is monitored during the model's trajectory and plotted for the three cases in Figure 15. The pockets of vapor maintain an essentially constant drag coefficient values during the time of trajectory for all the three models. Model 1 in red, model 2 in yellow, and model 3 in blue. As one can see, the solution differences between the models are very small, and it is clearly reflected by the relatively high volume fraction values obtained during the models motion. For example, the lowest volume fraction obtained in model 3, at time t=0.056 s is about 0.75 only. For this reason, the cavitation process has a low subscription on the integral drag confident values.

During the acceleration process, when t<0.02 s, the same drag values was generated by all the models. At time t>0.025 s cavities generated at the front, and as expected, the cavity formation first appeared in the spherical nose (model 1), where the flow acceleration is higher than the two other ogive type models. However, this is as far as we can go with this plot, and we cannot conclude that less drag is generated by an ogive type nose models. The three experimental and numerical comparisons were realistic, and even though more validation data (such as forces acting on the headform, or pressure values along the surface) would have been beneficial, this paper successfully demonstrated the cavitation's prediction on a complicated dynamic system.

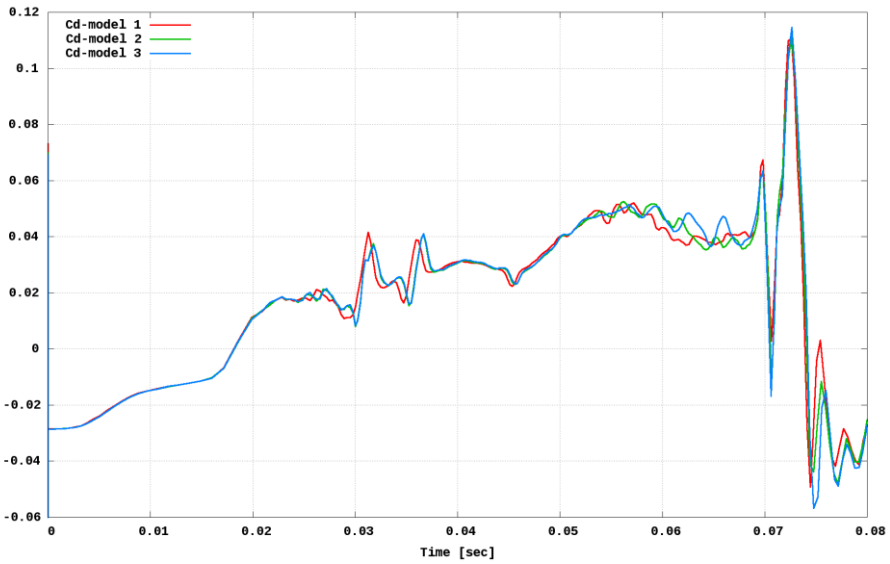

Fig. 15. Drag coefficient values with respect to simulated time for the three simulated models

VI. Summary

A new concept of experiment system to investigate high-speed underwater bodies was designed and built in Rafael.

Constant high velocities up to 30m/s were reached in tests. Bubble cavitation length was examined in different velocities and geometries. Results showed good agreement with CFD calculations. The validation was dine with the multiphase numerical model in OpenFOAM CFD solver platform. The main focus is to analyze the effect of different nose shapes on the cavitation pockets introduced during the bullet trajectory.

Further investigations on this field, mainly improvement of the measured experimental data, such as forces and moments acting on the bullet, pressure values along the headform surface, will provide additional data leading to a better understanding the effect the headform shape on the trailing cavitation process.

Future experimental research will investigate the stabilization of underwater bodies in different velocities and angles of attack. The system will be upgraded to include a balance to measure forces and moments in all directions operating on the cavitation and non-cavitation body during its motion. Besides drag and lift, it will also indicate the degree of unstable forces acting on the body and the possible implication in the case of a free moving vehicle under similar conditions. Scale effects will also be examines in this part of the research.

In this study, and experimental system for cavitation modeling is presented and validated with the multiphase numerical model in OpenFOAM CFD solver platform. The main focus is to analyze the effect of different nose shapes on the cavitation pockets introduced during the bullet trajectory.

References

[1] J. P. Franc, J. M. Michel, "Fundamentals of Cavitation", Kluwer Academic Publishers,

Dordrecht, 2004.

[2] C. E. Brennen, "Cavitation and Bubble Dynamics", Oxford University Press, New York, 1995.

[3] A.P. Keller, "Cavitation Scale Effects – Emprically found relations and the correlation. of cavitaion number and hydridynamic coefficients", cav2001, lecture.001, 2001

[4] D. A. Anderson, J. C. Tannehill and R. H. Pletcher, Computational Fluid Mechanics and Heat Transfer, New York: McGraw-Hill Book Company, 1984.

[5] P. J. Roache, K. Ghia and F. White, "Editorial Policy Statement on the Control of Numerical accuracy," *ASME Journal of Fluids Engineering*, p. 2, 1986.

[6] M. H. R. J., "Cavitation and Pressure Distribution:Head Forms at Zero Angle of Yaw," Institute of Hydraulix Research, Iowa, 1945.

[7] Y. CHEN and S. HEISTER, "Two-phase modeling of cavitated flows," *Computer and fluids,* vol. 24, pp. 799-809, 1995.

[8] R. D. Kunz, T. C. D. Boger and e. al., "Multi-phase CFD analysis of natural and ventilated cavitation about submerged bodies," in *Proceedings of FEDSM*, 1999.